IEEE Photonics Journal
An IEEE Photonics Society Publication

Open Access

Numerical Study of an Efficient Broadband Metamaterial Absorber in Visible Light Region

Volume 11, Number 3, June 2019

Tran Sy Tuan
Nguyen Thi Quynh Hoa

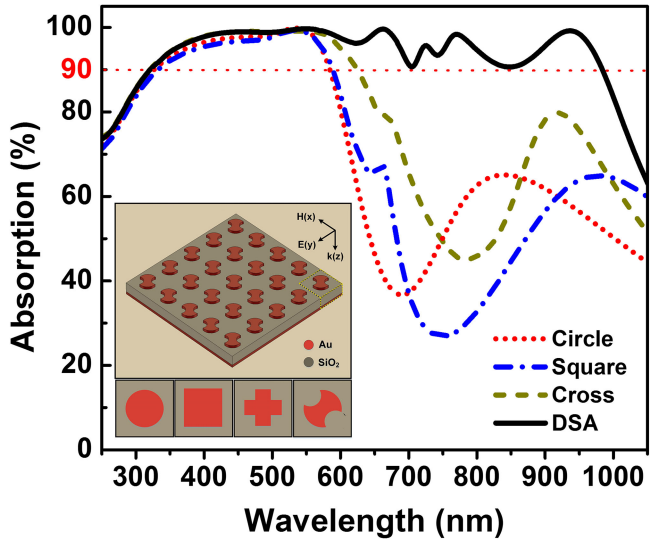

DOI: 10.1109/JPHOT.2019.2910806
1943-0655 © 2018 IEEE

Numerical Study of an Efficient Broadband Metamaterial Absorber in Visible Light Region

Tran Sy Tuan[1,2] **and Nguyen Thi Quynh Hoa** [1]

[1]School of Engineering and Technology, Vinh University, Vinh City, Vietnam
[2]Nguyen Tat Thanh University, Ho Chi Minh City, Vietnam

DOI:10.1109/JPHOT.2019.2910806

Manuscript received February 21, 2019; revised April 8, 2019; accepted April 9, 2019. Date of current version May 8, 2019. This research is funded by Vietnam National Foundation for Science and Technology Development (NAFOSTED) under Grant number 103.02-2017.367. Corresponding author: Nguyen Thi Quynh Hoa (email: ntqhoa@vinhuni.edu.vn).
This paper has supplementary downloadable material available at http://ieeexplore.ieee.org, provided by the author.

Abstract: We report a numerical study of a broadband metamaterial absorber in visible light region by utilizing a single layer of metal–dielectric–metal configuration. The absorption bandwidth and absorption performances are tailored by varying the resonator shapes and metal materials. The absorption bandwidth of the proposed metamaterial absorber (MA) structure is enhanced significantly with decreasing the order of rotational symmetry of the resonator shape. Using gold configuration, the twofold symmetry MA structure based on the double-sized axe shaped resonator exhibits the broadband absorption response over the entire visible light and apart of infrared spectrum range from 320 to 982 nm with absorptivity above 90% for both transverse electric and transverse magnetic polarizations. The physical mechanism of broadband absorption is explained by the current, electric, and magnetic distributions, significantly affected by the propagating surface and localized surface plasmon resonances. Furthermore, the high absorber performances of the twofold symmetry MA structure can be obtained over entire visible light region (400–700 nm) for both noble metal of gold and low-cost metal of nickel configurations, indicating the proposed absorber is a promising candidate for low-cost and large-scale fabricate device operated in visible light region.

Index Terms: Metamaterial, absorber, resonance, visible light.

1. Introduction

Metamaterial absorber (MA) has been intensively studied for both theoretical research and practical applications since Landy *et al.* proposed the microwave MA with near-unity absorbance in 2008 [1]. Generally, the metamaterial absorbers are designed based on the metal-insulation-metal (MIM) configuration because, compared to metal-insulation (MI) configuration, MIM configuration can be improved the absorption intensity of the MA [2], [3]. By the turning the shape and size of metal patch resonator, the MA was designed for different operation frequencies ranging from microwave to optics frequencies [1]–[19]. However, the controllable design of MA to obtain a wide operation bandwidth, insensitivity to light polarization, omni-directionality, and a considerable reduction in overall thickness has remained a challenging issue.

Recently, many efforts have been recently focused on the extension of absorption band and control of absorption frequency range in visible light regime for practical applications like photovoltaic device, photodetector, thermal emitter, and pulse generation [9]–[19]. To obtain broadband absorption, several approaches have been developed such as using a multi-shaped/sized architecture on planar structure and staking of metal/dielectric layers. Furthermore, an easy and controllable design that utilized a single layer asymmetry structure such as elongated shapes (eg. rectangular or ellipse) [20] and sharp corner shapes (eg. L or modified L shape) [6], [7] has proposed to broaden the absorption band. However, the asymmetry structure with a low order of rotational symmetry has commonly drawn the polarization sensitivity of MA, thereby limiting the applications of these structures that require the insensitive polarization characteristic. Therefore, the numerical and experimental design of MA in visible light regime have been mainly focused on the high order of rotational symmetry such as square, cross, cylinder shapes. For example, Aydin et al. [21] proposed a plasmonic absorber based on MIM configuration with a nanostructured top silver film composed of crossed trapezoidal array geometry which can realize an average absorption of 71% in the visible light range of 400 nm to 700 nm. The similar single layer MIM structure, Zhou et. al. [22] proposed a visible light absorber based on a quasi-periodic gold nanocone array, achieving an average front absorption of 87.4% and a corresponding rear absorptivity of 76.2% in the range 300–700 nm. Cui et al. presented a near-perfect absorber at visible frequency based on homogenous meta-surface nickel with a two-dimension cylinder array, which achieves average absorption at normal incidence are beyond 94% and 92% over the entire visible wavelength band from 400 nm to 700 nm, respectively [23]. Furthermore, Lei et al. proposed an ultra-broadband absorber formed by a periodic array of titanium-silica (Ti-SiO_2) cubes and aluminum bottom film which shows near 100% absorbing property in the range from 354 to 1066 nm [24]. Recently, Ghobadi et al. reported an optimized lattice arrangement for an ultra-broadband light absorber design based on an ellipse array that exhibits a near-perfect polarization independent of the shape of the top metallic patches of the absorber [20]. However, little information is available on the correlations between the order of rotational symmetry and metal material of resonator shapes and absorption characteristics of MA design.

In this work, for the first time, a simple strategy for designing of an efficient broadband MA in visible light regime has been proposed based on tailoring resonator shapes to obtain different orders of rotational symmetry and metal materials. The correlations between the order of rotational symmetry and absorption characteristics of the MA based on a single layer metal-dielectric-metal configuration and its physical mechanism are thoroughly numerically studied. Our simulation result shows that the high absorption over a broad absorption band range from 320 to 982 nm covering a significant visible to near-IR spectral window is obtained for the 2-fold symmetry MA structure based on a double-sized axe (DSA) shaped resonator using gold configuration. Furthermore, the absorption efficiency of the DSA shaped MA using both gold and nickel configurations is almost polarization insensitivity in visible light range (400 nm−700 nm) due to the contribution of the propagating surface plasmon (PSP) resonance.

2. Structure Design and Methods

Fig. 1 shows the proposed MA (Fig. 1(a)) with a magnified unit cell (Fig. 1(b)) and a top view of the unit cell (Fig. 1(c)). The MA structure consists of a periodic array of various surface geometries from asymmetry to symmetry shapes (DSA to cross, square, and circle) as seen in Fig. 1(c) and Fig. 1(d), respectively. The top and bottom layers are made of metal materials. The different metal materials are chosen to design the MA structure including noble metals (gold and silver) and common metals (nickel and aluminum). The top metallic layer is placed directly on the surface of a homogeneous silicon dioxide substrate. Meanwhile, the backside of dielectric layer is coved the same metallic material with the top layer acting as the ground to block the transmission. Thicknesses of the layers from top to bottom are 15 nm (t_1), 55 nm (h) and 15 nm (t_2), respectively. It was reported that the fabricated absorber with the very thin thickness of bottom metal layer of 8 nm showed over 90% absorption in range of visible and near-infrared regimes [25]. The geometrical dimensions of the

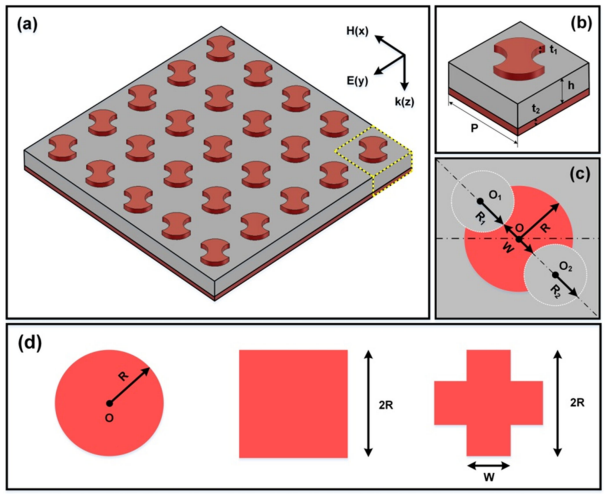

Fig. 1. Schematic of the proposed MA. (a) 3D-view. (b) Magnified 3D-view unit cell. (c) Top-view of a unit cell for double-sided axe resonator. (d) Top-view of various resonator shapes including circle, square, and cross (from left to right).

DSA unit cell are optimized using the numerical simulation based on frequency domain solver in a Computer Simulation Technology (CST) Microwave Studio. Periodic boundary conditions with Floquet-port are used in the x and y directions and the open condition in the z-direction. The Floquet-port was chosen to setup because Floquet mode can be applied to any periodical array whether rotated or mirrored [26]. As shown in Fig. 1(a), the electromagnetic (EM) wave is polarized so that the wave vector propagates to the front side of the MA in the $+$z direction with Zmax port. The S-parameters are extracted from Zmax port with respected to Amax in CST simulation. To increase the accuracy of the results and give a better prediction of the real performance of the fabricated device, the experimentally measured frequency-dependent dielectric constant of both metallic and dielectric materials has been imported to the numerical simulation. The dielectric constants of gold, silver, nickel are taken from Johnson [27], while aluminum from Palik [28], and silicon dioxide from Ghosh [29]. The aim of the optimized process is obtained the wider absorption bandwidth and the higher absorptivity in the visible region simultaneously. The optimized process is shown in Fig. 1S in the Supporting Information. Based on the simulated results, the optimized dimensional parameters of the unit cells for designing of the broadband MA are as follows: $P = 160$ nm, $R = 50$ nm, $R_1 = R_2 = 30$ nm, and $W = 40$ nm. The centers of the circles are $O\,(x = 0$ nm, $y = 0$ nm), $O_1(x = 35$ nm, $y = -35$ nm), $O_2(x = -35$ nm, $y = 35$ nm). The influence of structural parameters such as different structure shapes and metallic materials on the absorption characteristics of the MA is simulated and evaluated.

The absorption of the MA can be calculated by $A(\omega) = 1 - T(\omega) - R(\omega)$, where $A(\omega)$, $R(\omega)$ and $T(\omega)$ are the absorption, reflection, and transmission of the absorber, respectively. The transmission $T(\omega)$ and reflection $R(\omega)$ are determined from the frequency-dependent S-parameter $S_{11}(\omega)$ and $S_{21}(\omega)$, where $T(\omega) = |S_{21}(\omega)|^2$ and $R(\omega) = |S_{11}(\omega)|^2$. Because the thickness of the metal slab is thick enough to forbid the transmission of the incident wave ($T(\omega) = 0$), the absorption could be simplified to be $A(\omega) = 1 - R(\omega)$.

3. Results and Discussion

The absorption spectra of the MAs designed with various resonator shapes under normal incidence for both transverse electric (TE) and transverse magnetic (TM) polarizations are illustrated in Fig. 2. The absorption properties of these MAs are shown in Table 1. The metallic layer is made from gold. As expected, the absorption range of the proposed MAs can be controlled by varying the order

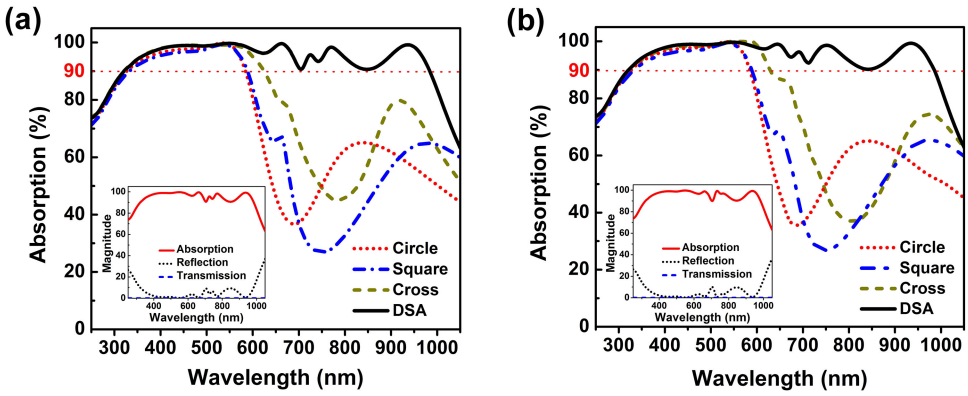

Fig. 2. Absorption spectra of the proposed MA with various resonator shapes under normal incidence for both TE and TM polarizations. The insets show the absorption, reflection, and transmission spectra of the DSA shaped MA.

TABLE 1
Absorption Properties of the MA Structure With Various Resonator Shapes Using Gold Configuration

Shape	Oder of rotational symmetry	Range with absorption > 90% absorption (nm)		Relative absorption bandwidth (RAB) (%)		Average absorption in range with absorption > 90% absorption (%)		
		TE	TM	TE	TM	A_{TE}	A_{TM}	A_{AVG}
Circle	∞	326-582	326-582	57%	57%	97.4	97.4	97.4
Square	4	331-587	331-587	57%	57%	96.7	96.7	96.7
Cross	4	320-624	323-626	64%	65%	97.9	98.1	98.0
DSA	2	320-982	320-982	102%	102%	97.0	97.0	97.0

of rotational symmetry of the resonator shapes. With decreasing the order of rotational symmetry, the absorption range is extended toward longer wavelengths due to the existence of different sized patch resonators, eg. the elongation of the geometry in one direction in the DSA shaped resonator [20]. The relative absorption bandwidth (*RAB*) is used to evaluate the absorption performance of the MAs which is calculated by using equation (1), where λ_U and λ_L are the upper and the lower frequencies of the absorption band with efficiency above 90% [7], [30].

$$RAB = 2\frac{\lambda_U - \lambda_L}{\lambda_U + \lambda_L} \tag{1}$$

As seen in Table 1, the largest and lowest *RAB* values are obtained in the MAs with DSA and circle resonator shapes, respectively. The absorption, reflection, and transmission spectra of the DSA shaped MA at normal incidence for both TE and TM polarizations are shown in the inset of Figs. 2(a) and (b), respectively. We note that the DSA shaped MA exhibits an absorption intensity higher than 90% in a wide wavelength range of 320-982 nm, covering from UV, visible to near-infrared regions and peak absorbilities of 98.97%, 99.68%, and 99.18% in UV (∼450 nm), visible (∼546 nm) and near-infrared regions (∼938 nm), respectively. The *RAB* of the DSA shaped MA reaches about 102%, which indicates a good wideband property. Furthermore, the absorption efficiencies of the proposed MA with various resonator shapes over the operating absorption band are calculated using equation (2), where $A(\lambda)$ is the wavelength response of the absorption coefficient. As seen in Table 1, the high average absorption (A) (>96%) is obtained for the MAs under both the TE (A_{TE})

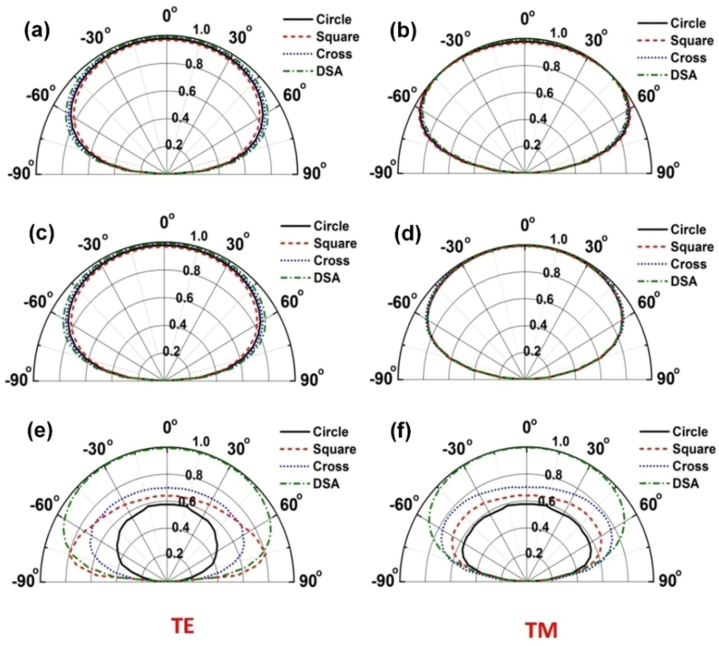

Fig. 3. Absorption spectra of the proposed absorber for various resonator shapes as a function of incident angle at several representative wavelengths of $\lambda = 450$ nm, 548 nm and 938 nm for (a), (c), (e) TE and (b), (d), (f) TM polarized waves, respectively.

and TM (A_{TM}) polarizations and their average (A_{AVG}).

$$A = \frac{1}{\lambda_U - \lambda_L} \int_{\lambda_L}^{\lambda_U} A(\lambda) d\lambda \tag{2}$$

To further determine the absorption performance of the MAs designed with various resonator shapes, the dependence of absorption properties on the incidence and polarization angles under both TE and TM polarizations is investigated. Fig. 3 plots the absorption spectra of the MAs with various resonator shapes as a function of incident angle at several representative wavelengths of $\lambda = 450$ nm, 548 nm and 938 nm for both TE and TM polarizations. The polar angle of the incident wave is varied from $-90°$ to $90°$ at the interval of $10°$ because the incident angle propagates to the front side of the MAs. One can see that the MA structures are dependent on the incident angle and the high absorption intensity maintains over a wide range of incident angles for both polarizations at wavelengths of 450 nm and 548 nm. At the wavelength of $\lambda = 450$ nm, the absorptivity of the circle and DSA shaped MAs is 0.98 and 0.99 at normal incidence and decreases slightly to 0.97 and 0.98 for TE polarization at an incident angle of $30°$, respectively. Even at incident angle of $60°$, the absorptivity could be as high as 0.87 and 0.89 for TE polarization, and 0.94 and 0.93 for TM polarization, respectively. The similar trend is obtained for $\lambda = 548$ nm. However, at the wavelength of $\lambda = 938$ nm, only DSA shaped MA exhibits the high absorption intensity due to its resonant feature and that exists as high as 0.94 under TE polarization and 0.89 under TM polarization for incident angle of $60°$.

The physical mechanism of MA is generally based on the localized surface plasmon (LSP) resonance [31], [32], the propagating surface plasmon (PSP) resonance [33], and the combination of both the LSP and PSP resonances [24], [34]. The distributions of current density, electric and magnetic fields are used to explain the absorption mechanism of the MA structure [24], [31]–[34]. Figure. 4 shows the current density and the distributions of electric and magnetic field of the DSA-shaped MA under the TE polarization at various resonant wavelengths of 450 nm, 546 nm and 938 nm in the YOZ plane. As seen in Figs. 4(a)–(c), the current density is mainly concentrated

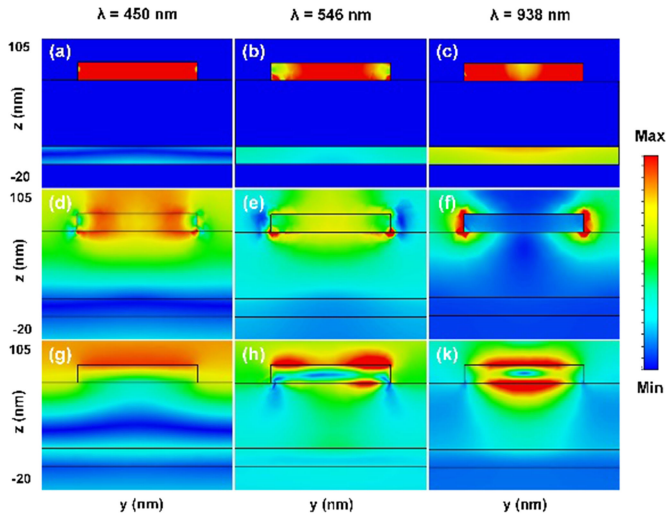

Fig. 4 (a), (b), (c) Current density and distributions of (d), (e), (f) electric field and magnetic field on the YOZ plane of a unit cell at various resonant wavelengths of 450 nm, 548 nm, and 938 nm, respectively. The y-direction is taken form −80 nm to 80 nm.

in the metallic resonator and on top of the metallic ground plane, which confirms the surface plasmon resonance. It was reported that the surface plasmon resonance can be attributed to the wideband absorption phenomenon [24]. Furthermore, the electric current distributes in the top and bottom metal layers that means the origins of the energy loss in the dielectric layer which result in the broadband absorption [24]. The electric field distribution is localized around the metal corners between the neighbor unit cells, as seen in Figs. 4(d)–(f). Furthermore, the electric field is a strong coupled in to air-slot at that resonant wavelength of 938 nm, indicating that surface plasmon polaritons (SPPs) are excited in the structure [20], [24]. The distributions of the magnetic field at these resonant wavelengths are shown in Figs. 4(g)–(k). The distributions of the magnetic field of the MA for various resonant wavelengths are significantly different. It was reported that the different distributions of the magnetic field is due to different types of resonances such as LSP and PSP [20], [24], [31]–[34]. At the resonant wavelength of 938 nm, the localized magnetic field within the gap between the top metallic resonator and the metallic ground plane results in LSP resonance [24], [31], [32], [34]. Meanwhile, the magnetic field is not only accumulated in the metallic resonator but also spread through the neighbor unit cells at the resonant wavelength of 450 nm, indicating that the absorption around 450 nm results from PSP resonance [24], [33], [34]. Both the LSP and PSP resonances are excited at the resonant wavelength of 546 nm as evidenced by the distribution of magnetic field in Fig. 4(h). Both the LSP and PSP resonances are excited at the resonant wavelength of 546 nm as evidenced by the distribution of magnetic field in Fig. 4(h).

Besides the order of rotational symmetry of resonator shape, the metal materials are also found to be affected on absorption performance of the MA as shown in Fig. 5 and summarized in Table 2. The data for the DSA shaped MA are gathered at normal incidence. It can be observed that the variation of the metals not only influences the absorption range and bandwidth but also affects the absorption efficiency the DSA shaped MAs. Meanwhile, the absorption properties are almost unchanged for both TE and TM polarizations. The MA designed based on gold configuration shows the widest operating absorption band along with a high average absorption over both that band and visible light range, though these highest absorbencies are obtained for nickel configuration. We note that the DSA-shaped MAs give the average absorbance higher than 90% for both noble metals (gold and silver) and common metals (nickel and aluminum), and the nearly perfect absorbance (99%) for nickel and gold in the visible light range.

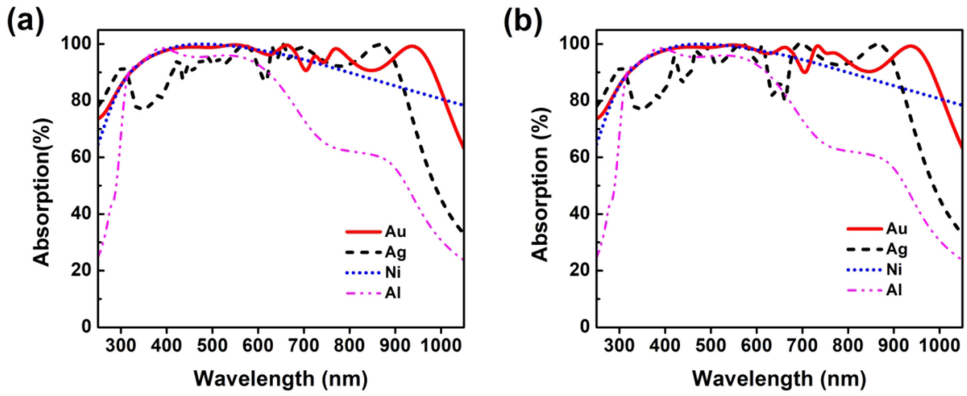

Fig. 5. Absorption efficiencies of the proposed MAs designed with various metals under normal incidence for (a) TE and (b) TM polarizations.

TABLE 2
Absorption Properties of the DSA Shaped MA Structure With Various Metals

	Range with absorption > 90% absorption (nm)		Average absorption in range with absorption > 90% absorption (%)			Average absorption in visible light range of 400 - 700 nm (%)		
Metal	TE	TM	A_{TE}	A_{TM}	A_{AVG}	A_{TE}	A_{TM}	A_{AVG}
Gold	320-982	320-982	97.0	97.0	97.0	99.0	99.0	99.0
Silver	411-907	411-907	95.7	95.3	95.5	95.1	94.2	94.7
Nickel	320-799	320-799	97.1	97.1	97.1	99.1	99.1	99.1
Aluminum	316-620	316-620	95.8	95.9	95.9	92.5	92.5	92.5

The broadband absorbance of the MA can realize by the impedance nearly matched to that of the free space in the operating absorption band and surface plasmon resonances [2]. It is evidenced by the real part of impedance is near unity, while the imaginary part is close to zero in the whole range. The real and imaginary parts of the retrieved effective impedance (Z) of the MAs are calculated by using S parameters (3) [35]–[37].

$$Z = \sqrt{\frac{(1+S_{11})^2 - S_{21}^2}{(1-S_{11})^2 - S_{21}^2}} = \frac{1+S_{11}}{1-S_{11}} \tag{3}$$

Furthermore, based on the equivalent RLC circuit model of the MIM three-layer structure, the input impedance of the MA is dependent on the intrinsic properties of both materials (metal and dielectric) and resonator shapes [2], [31], [38]. By tailoring the above parameters, the impedance matching band can be controlled, thus the tunable absorption band of the MA can be obtained. Notably, the impedance of the MA is the complex impedance in which the real part represents resistance (R) and the imaginary part represents reactance (X). Resistance is always positive, while reactance can be either positive or negative due to that element's inductance or capacitance, respectively. Resistance in a circuit dissipates power as heat, while reactance stores energy in the form of an electric or magnetic field. That means the negative imaginary part of the impedance can be observed when the reactance of the MA structure is capacitance that stores electrical energy in the form of an electric field. Meanwhile, the imaginary part of the impedance is positive when the reactance of the MA structure is inductance that stores electrical energy in the form of an electric field. Fig. 6 shows the extracted effective impedance of the DSA shaped MA designed with various

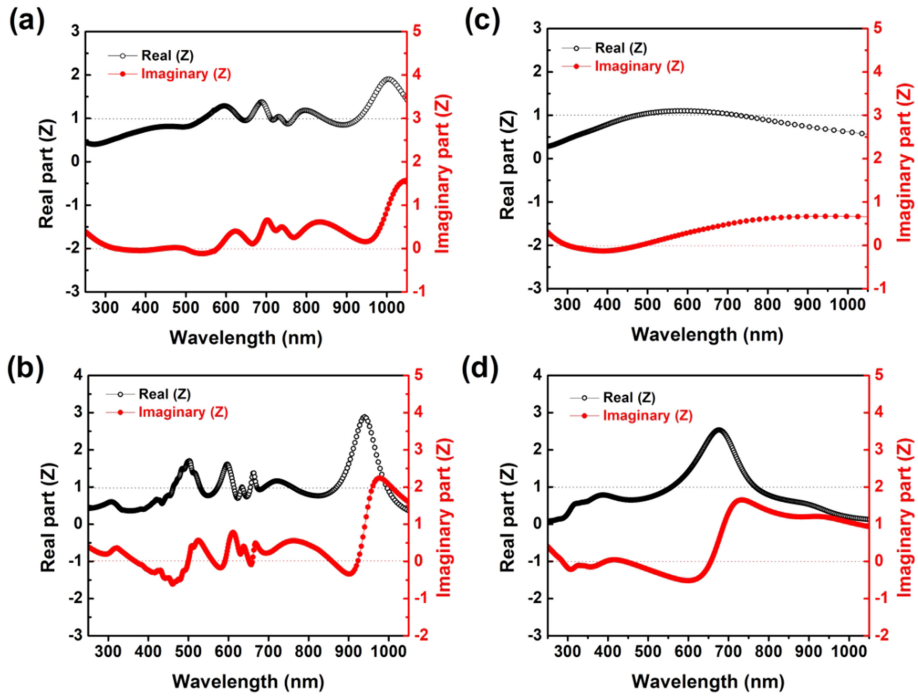

Fig. 6. The frequency response of the extracted effective input impedance (Z) of the DSA shaped MA designed with various metals under normal incidence

metals. As seen in Fig. 6, due to the change of dispersion property of metals, the variation of the matching wavelength range can be observed for the MAs with different metals. Thus, the perfect absorption can be collected in the broader or narrower absorption bandwidth according to the metal materials used for designing the MAs. Similarly, the changing of the position and the intensity of the broadband absorption of the MAs based on gold configuration with different resonator shapes are also observed as shown in Fig. 2.

We also investigated the effect of the incident and polarization angle on the absorption efficiency of the DSA-shaped MA with various metals for both TE and TM polarizations. The average absorption is calculated in the visible light range of 400–700 nm. As shown in Fig. 7, the average absorption is sensitive with both the incident and polarization angle due to the asymmetry structure of DSA resonator shape. However, the DSA shaped MAs possess the average absorption higher 80% with an incident angle up to 60° for both polarizations, as seen in Figs. 7(a) and (b). It is not surprising that the average absorption decreases sharply with increasing the polarization from 0 to 45° and then increases with further increasing the polarization angle from 45° to 90° as observed in case of silver and aluminum. However, interestingly, it seems to be slightly affected by the polarization angle for the MAs with gold and nickel; and these MAs can retain the average absorber as high as 97.2 and 99.1 for TE polarization and 94.4 and 97.7 for TM polarization, respectively (Figs. 7(c) and (d)). Meanwhile, at the long wavelength in the range of 700-938 nm, the absorption spectra are strongly affected by polarization for both gold and nickel. The absorption spectra of the DSA shaped MA based on gold configuration as a function of polarization angle under both TE and TM polarizations as shown in Fig. S2 in the Supporting Information. It can be clear that the polarization insensitivity in the MAs can be related to the absorption mechanism. In visible light range, the PSP resonance that occurred in the MAs in visible light range can be the major reason for the observed polarization insensitivity in 2-fold symmetry of resonator shape for both gold and nickel. Meanwhile, the LSP resonance is excited in the MAs at the long wavelength cannot be attributed to the polarization insensitivity. Therefore, it is crucial to tailor the metal materials and resonator shapes for designing the low-cost MA structure achieved good absorption performances.

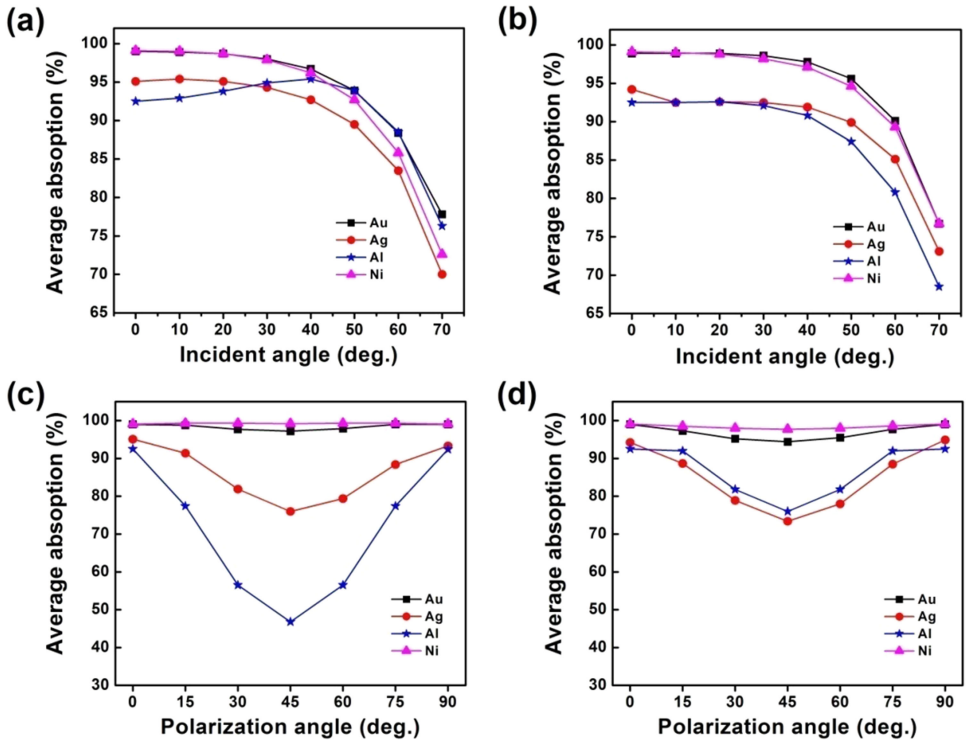

Fig. 7. Average absorption as a function of incident and polarization angle for (a, c) TE and (b, d) TM polarizations, respectively.

4. Conclusion

A tailoring design of a broadband MA in visible light region based on a single layer of metal-dielectric-metal configuration was studied numerically. The absorption bandwidth and absorption performances were controlled by turning the shape and metal material of resonator shape. The absorption band was significantly increased with decreasing the order of rotational symmetry of patch resonator. Using the gold configuration, the broadband absorption response of the MA structure based on the 2-fold symmetry of the DSA shaped resonator over the entire visible light and apart of infrared spectrum range from 320 nm to 982 nm with absorptivity above 90% for both TE and TM polarizations was obtained. The physical mechanism of broadband absorption was investigated by the current, electric and magnetic distributions, contributed by propagating surface plasmon (PSP) and localized surface plasmon (LSP) resonances. In addition, the high absorber performances of DSA shaped MA structure over entire visible light region (400 nm–700 nm) can be achieved for both noble metal of gold and low-cost metal of nickel configurations, suggesting that the proposed absorber is a promising candidate for visible light applications.

References

[1] N. I. Landy, S. Sajuyigbe, J. J. Mock, D. R. Smith, and W. J. Padilla, "Perfect metamaterial absorber," *Phys. Rev. Lett.*, vol. 100, no. 20, 2008, Art. no. 207402.
[2] A. Ghobadi, H. Hajian, A. R. Rashed, B Butun, and E Ozbay, "Tuning the metal filling fraction in metal-insulator-metal ultra-broadband perfect absorbers to maximize the absorption bandwidth," *Photon. Res.*, vol. 6, no. 3, pp. 168–176, 2018.
[3] Y. Chen, J. Dai, M. Yan, and M. Qiu, "Metal-insulator-metal plasmonic absorbers: Influence of lattice," *Opt. Exp.*, vol. 22, no. 25, pp. 30807–30814, 2014.
[4] D. T. Viet *et al.*, "Perfect absorber metamaterials: Peak, multi-peak and broadband absorption," *Opt. Commun.*, vol. 322, pp. 209–213, 2014.

[5] N. T. Q. Hoa, P. H. Lam, P. D. Tung, T. S. Tuan, and H. Nguyen, "Numerical study of a wide-angle and polarization-insensitive ultrabroadband metamaterial absorber in visible and near-infrared region," *IEEE Photon. J.*, vol. 11, no. 1, Feb. 2019, Art. no. 4600208.
[6] D. Sood, and C. C. Tripathi, "A wideband ultrathin low profile metamaterial microwave absorber," *Microw. Opt. Technol. Lett.*, vol. 57, no. 12, pp. 2723–2728, 2015.
[7] N. T. Q. Hoa, P. H. Lam, and P. D.Tung, "Wide-angle and polarization-independent broadband microwave metamaterial absorber," *Microw. Opt. Technol. Lett.*, vol. 59, no. 5, pp. 1157–1161, 2017.
[8] T. Beeharry, R. Yahiaoui, K. Selemani, and H. H. A. Ouslimani, "Dual layer broadband radar absorber to minimize electromagnetic interference in Radomes," *Sci. Rep.*, vol. 8, 2018, Art. no. 382.
[9] N. T. Q. Hoa, P. D. Tung, P. H. Lam, N. D. Dung, and N. H. Quang, "Numerical study of an ultrabroadband, wide-angle, polarization-insensitivity metamaterial absorber in the visible region," *J. Electron. Mater*, vol. 47, no. 5, pp. 2634–2639, 2018.
[10] D. Wu *et al.*, "Numerical study of an ultra-broadband near-perfect solar absorber in the visible and near-infrared region," *Opt. Lett.*, vol. 42, no. 3, pp. 450–453, 2017.
[11] H. A. Atwater and A. Polman, "Plasmonics for improved photovoltaic devices," *Nat. Mater*, vol. 9, no. 3, pp. 205–213, 2010.
[12] S. Mubeen, J. Lee, W. Lee, N. Singh, G. D. Stucky, and M. Moskovits, "On the plasmonic photovoltaic," *ACS Nano*, vol. 8, no. 6, pp. 6066–6073, 2014.
[13] A. Vora, J. Gwamuri, N. Pala, A. Kulkarni, J. M. Pearce, and D. Ö. Güney, "Exchanging ohmic losses in metamaterial absorbers with useful optical absorption for photovoltaics," *Sci. Rep.*, vol. 4, 2014, Art. no. 4901.
[14] M. D. Goldflam *et al.*, "Enhanced infrared detectors using resonant structures combined with thin type-II super lattice absorbers," *Appl. Phys. Lett.*, vol. 109, no. 25, 2016, Art. no. 251103.
[15] W. Li, and J. Valentine, "Metamaterial perfect absorber based hot electron photodetection," *Nano Lett.*, vol. 14, no. 6, pp. 3510–3514, 2014.
[16] H. Wang, and L. Wang, "Perfect selective metamaterial solar absorbers," *Opt. Exp.*, vol. 21, no. S6, pp. A1078–A1093, 2013.
[17] Y. Gong *et al.*, "Highly efficient and broadband mid-infrared metamaterial thermal emitter for optical gas sensing," *Opt. Lett.*, vol. 42, no. 21, pp. 4537–4540, 2017.
[18] D. Wu *et al.*, "Numerical study of a wide-angle polarization independent ultra-broadband efficient selective metamaterial absorber for near-ideal solar thermal energy conversion," *RSC Adv.*, vol. 8, no. 38, pp. 21054–21064, 2018.
[19] D. Li *et al.*, "Polarization and thickness dependent absorption properties of black phosphorus: new saturable absorber for ultrafast pulse generation," *Sci. Rep.*, vol. 5, 2015, Art. no. 15899.
[20] A. Ghobadi *et al.*, "Visible light nearly perfect absorber: an optimum unit cell arrangement for near absolute polarization insensitivity," *Opt. Exp.*, vol. 25, no. 22, pp. 27624–27634, 2017.
[21] K. Aydin, V. E. Ferry, R. M. Briggs and H. A. Atwater, "Broadband polarization-independent resonant light absorption using ultrathin plasmonic super absorbers," *Nat. Commun.*, vol. 2, 2011, Art. no. 517.
[22] L. Zhou *et al.*, "Broadband bidirectional visible light absorber with wide angular tolerance," *J. Mater. Chem. C*, vol. 4, no. 2, pp. 391–397, 2016.
[23] Y. Zhou, M. Luo, S. Shen, H. Zhang, D. Pu, and L. Chen, "Cost-effective near-perfect absorber at visible frequency based on homogenous metasurface nickel with two-dimension cylinder array," *Opt. Exp.*, vol. 26, no. 21, pp. 27482–27491, 2018.
[24] L. Lei, S. Li, H. Huang, K. Tao, and P. Xu, "Ultra-broadband absorber from visible to near-infrared using plasmonic metamaterial," *Opt. Exp.*, vol. 26, no. 5, pp. 5686–5693, 2018.
[25] D. Lee *et al.*, "Polarization-sensitive tunable absorber in visible and near-infrared regimes," *Sci. Rep*, vol. 8, 2018, Art. no. 12393.
[26] C. Gong *et al.*, "Broadband terahertz metamaterial absorber based on sectional asymmetric structures," *Sci. Rep.*, no. 6, 2016, Art. no. 32466.
[27] P. B. Johnson and R. W. Christy, "Optical constants of the noble metals," *Phys. Rev. B*, vol. 6, no. 12, 1972, Art. no. 4370.
[28] E. D. Palik, *Handbook of Optical Constants of Solids.* New York, NY, USA: Academic Press, 1985.
[29] G. Ghosh, "Dispersion-equation coefficients for the refractive index and birefringence of calcite and quartz crystals," *Opt. Commun*, vol. 163, no. 1–3, pp. 95–102, 1999.
[30] F. Ding, Y. Cui, X. Ge, Y. Jin, and S. He, "Ultra-broadband microwave metamaterial absorber," *Appl. Phys. Lett.*, vol. 100, 2012, Art. no. 103506.
[31] Y. Zhang *et al.*, "Vapor-deposited amorphous metamaterials as visible near-perfect absorbers with random non-prefabricated metal nanoparticles," *Sci. Rep.*, vol. 4, 2014, Art. no. 4850.
[32] Y. Nishijima, A. Balcytis, S. Naganuma, G. Seniutinas, and S. Juodkazis, "Tailoring metal and insulator contributions in plasmonic perfect absorber metasurfaces," *ACS Appl. Nano Mater.*, vol. 1, pp. 3557–3564, 2018.
[33] Q. Li *et al.*, "Tunable plasmonic absorber based on propagating and localized surface plasmons using metal-dielectric-metal structure," *Plasmonics*, vol. 12, no. 4, pp. 1037–1043, 2017.
[34] F. Ding, J. Dai, Y. Chen, J. Zhu, Y. Jin, and S. I. Bozhevolnyi, "Broadband near-infrared metamaterial absorbers utilizing highly lossy metals," *Sci. Rep.*, vol. 6, 2016, Art. no. 39445.
[35] D. R. Smith, D. C. Vier, T. Koschny, and C. M. Soukoulis, "Electromagnetic parameter retrieval from inhomogeneous metamaterials," *Phys. Rev. E*, vol. 71, no. 3, 2005, Art. no. 036617.
[36] S. Bhattacharyya and K. V. Srivastava, "Triple band polarization-independent ultra-thin metamaterial absorber using electric field-driven LC resonator," *J. App. Phys.*, vol. 115, no. 6, 2014, Art. no. 064508.
[37] N. T. Q. Hoa, T. S. Tuan, L. T. Hieu and B. L. Giang, "Facile design of an ultra-thin broadband metamaterial absorber for C-band applications," *Sci. Rep.*, vol. 9, 2019, Art. no. 468.
[38] Z. Li, L. Stan, D. A. Czaplewski, X. Yand, and J. Gao, "Wavelength-selective mid-infrared metamaterial absorbers with multiple tungsten cross resonators," *Opt. Exp.*, vol. 26, no. 5, pp. 5616–5631, 2018.